Available online at www.sciencedirect.com

SciVerse ScienceDirect

journal homepage: www.elsevier.com/locate/he

Design of a mobile PEM power backup system through detailed dynamic and control analysis

P. Iora [a,*], J. Thangavelautham [b]

[a] Dipartimento di Ingegneria Meccanica e Industriale, Università degli Studi di Brescia, Via Branze 38, 25123 Brescia, Italy
[b] Department of Mechanical Engineering, Massachusetts Institute of Technology, 77 Massachusetts Avenue, Cambridge, Massachusetts, USA

ARTICLE INFO

Article history:
Received 5 June 2012
Received in revised form
13 August 2012
Accepted 14 August 2012
Available online 12 September 2012

Keywords:
PEM fuel cell
Mathematical modeling
System engineering
Dynamic and control analysis
Uninterruptable power units

ABSTRACT

In this paper we present a one dimensional dynamic model of a PEM fuel cell applied to the design of a mobile backup system for uninterruptable power units. The fuel cell is modeled using a finite difference approach where mass and energy balance equations are applied locally together with the pertinent equations of the electrochemical model yielding the profiles of any relevant thermodynamic and electrochemical cell variable. An accurate analysis of the membrane humidification is included based on state of the art models available in literature.

In this system the fuel cell is fed by pure hydrogen taken from a lithium hydride hydrogen storage while ambient air is supplied to the cathode by an inverter-fed electric motor fan. A preliminary design of the main components is provided for a target operating time of 48 h. Dynamic simulations are then carried out applying to the fuel cell the actual electricity load of a computer file server that was experimentally measured by a power measurement device over a period of 0.5 h. Results of the simulations show that with an appropriate choice of the controllers parameters it is possible to maintain effective cell operation under different load variations keeping the key variables of the fuel cell within the desired set point targets.

1. Introduction

The proton exchange membrane (PEMs) fuel cells are considered a promising power source in many applications as they show several advantageous properties such as fast startup, high efficiency, low-temperature operation, high power density and favorable power-to-weight ratio. Typical applications are transportation, stationary cogeneration and portable power [1–7]. Recent advances in the cell technology have also opened the way for commercialization in the field of Uninterruptable Power Supply (UPS) and backup power market, showing the possibility to reach wide scale application [8–12]. Normally these systems are based on the combination of PEM fuel cells with electricity storage devices such batteries or supercapacitors yielding the so called hybrid power sources that make the best use of the advantages of each individual device [13]. Recently also, some studies have focused on modeling and control of hybrid UPS systems [13–17]. The main function of UPS is that once the utility grid is shut down, it could immediately supply power to sustain machine operation for a period of time until power supply is back to normal. When employed to supply power units in off-grid systems, the challenge is to meet the power demands of varying loads. The control system has to ensure that the key parameters of the fuel cell are in their optimal values to allow an effective operation and avoid degradation that could

* *Corresponding author*. Tel.: +39 0303715570.
E-mail address: paolo.iora@ing.unibs.it (P. Iora).
0360-3199/$ – see front matter
http://dx.doi.org/10.1016/j.ijhydene.2012.08.068

damage the fuel cell stack. One of the important tools in the optimization study of fuel cell performances is computational modeling, which can be used to reveal the fundamental phenomena taking place in the fuel cell, predict performances under different operating conditions, show the distribution profiles of various dependent variables and ultimately optimize the design of the fuel cell system. There are many published mathematical models of PEM fuel cell in the literature with various level of complexity and they could be classified according to Ref. [18] into three categories: (i) steady state mathematical models based on empirical equations, (ii) one dimensional dynamical models and (iii) two and three dimensional models based on Navier–Stokes equations. A good review of these models and their relevant calibration parameters can be found in [19].

In this paper we present a one dimensional finite difference dynamic model of a PEM fuel cell applied to the design of a mobile PEM power backup system. The degree of detail of the model can be considered appropriate for the purpose of this study, while more complex solutions (i.e. two or three dimensional analysis of the fuel cell) although more accurate, are generally unpractical in term of computational time when transient analysis are carried out at system level. The PEM model is integrated with the necessary Balance of Plant (BoP) components model and it is employed to prove the feasibility of a PEM system for use as a back up power supply. For this purpose the actual electricity load of a computer file server was experimentally measured by a power measurement device and applied to the fuel cell over a period of 0.5 h. Dynamic simulations are carried out with Aspen Custom Model [20] to determine an appropriate control strategy and maintain the fuel cell close to optimized operating conditions under the load changes.

2. PEM model development

A fuel cell unit normally consists of many cells combined to reach the desired power level. Each cell is composed of several channels depending on the manufacturing technology. Since the number of flow channels in the bipolar plate can be quite large, a numerical simulation of the whole cell results in a computationally demanding task. Therefore, a typical element is usually separated from the fuel cell in the computational domain. Then, based on the assumption that the process is periodic from channel to channel, such an element can be regarded as the representation of the entire fuel cell unit [21,22].

Following this approach, in this model, the planar co-flow unit cell is divided axially in a desired number of intervals following a finite difference modeling method. Each interval consists of six sub-sections as shown in Fig. 1: anode channel, cathode channel, solid phase (representing the membrane, the electrodes, catalysts and the gas diffusion layer) the anode and cathode bipolar plate and a refrigerant fluid channel that removes the heat from the fuel cell. It is worth noting that this approach provides a better representation of the actual cell assembly with respect to existing along the channel models [23–25] where the bipolar plates are not considered in the calculation domain and the cooling fluid is in direct contact with the Membrane Electrode Assemblies (MEA). Within each interval, mass and energy balance equations are applied locally together with the pertinent equations of the electrochemical model. An accurate analysis of the membrane humidification is included, similar to the approach presented in [23,24,26]. The model's governing equations are reported in sections 2.1–2.3.

2.1. Mass balance

For the mass balance in the flow channels, the chemical species considered are H_2 and H_2O for the anode and O_2, N_2 and H_2O for the cathode. Mass balance equations and the corresponding boundary conditions are reported below:

Anode channel:

$$\frac{\partial C_{H_2,V}}{\partial t} = -u_V \frac{\partial C_{H_2,V}}{\partial x} - \frac{j}{2FH_V} \tag{1}$$

$$C_{H_2,V}\big|_{x=0} = C^0_{H_2,V} \tag{2}$$

$$\frac{\partial C_{H_2O,V}}{\partial t} = -u_V \frac{\partial C_{H_2O,V}}{\partial x} - \alpha \frac{j}{FH_V} \tag{3}$$

$$C_{H_2O,V}\big|_{x=0} = C^0_{H_2O,V} \tag{4}$$

Cathode channel:

$$\frac{\partial C_{O_2,III}}{\partial t} = -u_{III} \frac{\partial C_{O_2,III}}{\partial x} - \frac{j}{4FH_{III}} \tag{5}$$

$$C_{O_2,III}\big|_{x=0} = C^0_{O_2,III} \tag{6}$$

$$\frac{\partial C_{N_2,III}}{\partial t} = -u_{III} \frac{\partial C_{N_2,III}}{\partial x} \tag{7}$$

$$C_{N_2,III}\big|_{x=0} = C^0_{N_2,III} \tag{8}$$

$$\frac{\partial C_{H_2O,III}}{\partial t} = -u_{III} \frac{\partial C_{H_2O,III}}{\partial x} + \frac{j}{2FH_{III}} + \alpha \frac{j}{FH_{III}} \tag{9}$$

$$C_{H_2O,III}\big|_{x=0} = C^0_{H_2O,III} \tag{10}$$

It is worth noting that the equations above completely describe the water balance on the fuel cell considering the effect of (i) water generated by the electrochemical reaction (second term on the right hand side in Eq. (9)); (ii) net water flow through the membrane due to the combined effect of osmotic drag and back diffusion by concentration and pressure gradients (second term on the right hand side in Eq. (3) and the third term on right hand side of Eq. (9)). The latter contribution is modeled through the definition of the parameter α calculated according to [23] as:

$$\alpha = n_d - \frac{F}{j} D^* \frac{c_{w,c} - c_{w,a}}{H_{IV}} - \frac{c_{w,c} + c_{w,a}}{2} \frac{k_p}{\mu} \frac{F}{j} \frac{P_{w,c} - P_{w,a}}{H_{IV}} \tag{11}$$

where the various terms of Eq. (11) are taken from Refs. [23,24] and calculated with the expressions reported in Table 1.

Any H_2O phase change (i.e. condensation or evaporation) in the flow channels is taken into account on the basis of the local conditions (H_2O partial pressure and local temperature).

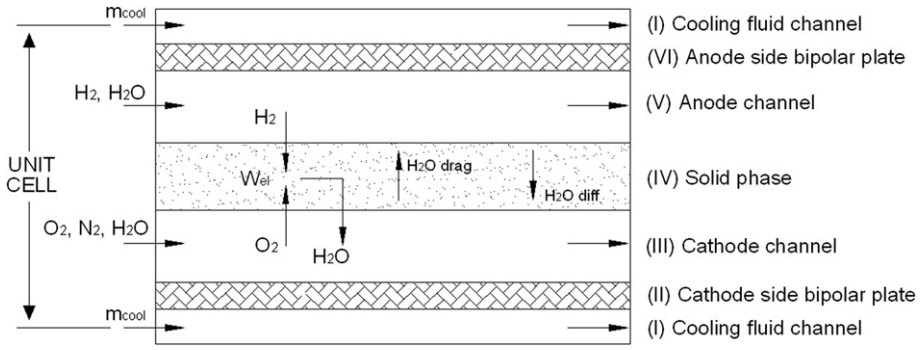

Fig. 1 – Finite portion of the PEM.

Ideal gas behavior is assumed at anode and cathode streams to determine the inlet molar concentrations at feed conditions.

2.2. *Energy balance*

The energy balances and boundary conditions are given by Eqs. (16)–(27). The energy balances consider the thermal fluxes between the gas streams and the solid parts of the cell to be fully described by convection assuming a constant heat transfer coefficient. The thermal fluxes along the solid parts of the cell are modeled using Fourier's law of heat conduction. Given the relatively low operating temperature, radiative heat exchange is neglected. The electrochemical reactions take place in the solid portion of the PEM as shown in Fig. 1. Therefore, the enthalpy fluxes associated with the flow of oxygen and hydrogen to the solid phase and the flow of water from the solid phase are taken into account in the solid heat balance (fourth term on the right-hand side of Eq. (22)) while the second term on the right-hand side of Eqs. (20) and (24) refers to the enthalpy fluxes pertinent to the cathode and anode channels. Similarly, the enthalpy fluxes associated with the net water migration through the membrane owing to the effect of water osmotic drag and back diffusion by concentration and pressure gradients are accounted in Eq. (20), (third term on right hand side), (22) (fifth term on right hand side) and (24) (third term on right hand side). The flow internal energy, e, in Eqs. (20) and (24) is calculated, according to the definition, as $e = h - P/\rho$ where, assuming ideal gas behavior, the enthalpy h is obtained for each species as a function of the local temperature $h_i = \Delta h_i^0 + \int_{T_{ref}}^{T} c_p \cdot dT$ being Δh_i^0 the enthalpy of formation of specie i. In spite of the temperature gradient expected along the cell (for the conditions considered here, about 40 °C for the cathodic stream and 10 °C for the solid parts and anodic stream), heat capacities and densities of solid structures and bipolar plate, as well as gas velocities are determined for the inlet conditions and are kept constant along the cell, in order to achieve a more computationally tractable model. This assumption is reported valid for the previously developed models [21] and is thus also considered applicable in this case.

Table 1 – Equations required to compute the terms in Eq. (11).

$$n_d = \begin{cases} 0.0049 + 2.02a_a - 4.53a_a^2 + 4.09a_a^3 & a_a \le 1 \\ 1.59 + 0.159(a_k - 1) & a_a > 1 \end{cases} \quad (12)$$

$$a_a = \frac{x_{w,a}P}{P_{w,a}^{sat}} = \left(\frac{M_{w,a}^{v}}{M_{w,a}^{v} + M_{H_2}}\right)\frac{P}{P_{w,a}^{sat}}$$
$$a_c = \frac{x_{w,c}P}{P_{w,c}^{sat}} = \left(\frac{M_{w,c}^{v}}{M_{w,c}^{v} + M_{O_2} + M_{N_2}}\right)\frac{P}{P_{w,c}^{sat}} \quad (13)$$

$$c_{w,k} = \begin{cases} \frac{\rho_{m,dry}}{W_{m,dry}}(0.043 + 17.8a_k - 39.85a_k^2 + 36a_k^3) & a_k \le 1 \; k = a,c \\ \frac{\rho_{m,dry}}{W_{m,dry}}(14 + 1.4(a_k - 1)) & a_k > 1 \; k = a,c \end{cases} \quad (14)$$

$$D^* = n_d D_0 \exp\left[2416\left(\frac{1}{303} - \frac{1}{T_{IV}}\right)\right] \quad (15)$$

Cooling fluid channel (I):

$$\rho_I c_{p,I}\frac{\partial T_I}{\partial t} = -\frac{\dot{m}_I c_{p,I}}{WH_I}\frac{\partial T_I}{\partial x} + U_{I,II}(T_{II} - T_I)\frac{1}{H_I} + U_{I,VI}(T_{VI} - T_I)\frac{1}{H_I} \quad (16)$$

$$T_I|_{x=0} = T_I^0 \quad (17)$$

Cathode side bipolar plate (II):

$$\rho_{II} c_{p,II}\frac{\partial T_{II}}{\partial t} = \lambda_{II}\frac{\partial^2 T_{II}}{\partial x^2} + U_{I,II}(T_I - T_{II})\frac{1}{H_{II}} + U_{II,III}(T_{III} - T_{II})\frac{1}{H_{II}} \quad (18)$$

$$\lambda_{II}\frac{\partial T_{II}}{\partial x}\Big|_{x=0} = U_{inf}(T_{II} - T_{inf}) \quad \lambda_{II}\frac{\partial T_{II}}{\partial x}\Big|_{x=L} = -U_{inf}(T_{II} - T_{inf}) \quad (19)$$

Cathode channel (III):

$$\frac{\partial C_{III} e_{III}}{\partial t} = -u_{III}\frac{\partial C_{III} h_{III}}{\partial x} + \frac{j}{2F}\left(h_{H_2O,IV} - \frac{1}{2}h_{O_2,III}\right)\frac{1}{H_{III}} + \alpha\frac{j}{F}h_{H_2O,IV}\frac{1}{H_{III}} + U_{II,III}(T_{II} - T_{III})\frac{1}{H_{III}} + U_{III,IV}(T_{IV} - T_{III})\frac{1}{H_{III}} \quad (20)$$

$$T_{III}|_{x=0} = T^0_{III} \quad (21)$$

Solid phase (IV):

$$\rho_{IV} c_{p,IV} \frac{\partial T_{IV}}{\partial t} = \lambda_{IV} \frac{\partial^2 T_{IV}}{\partial x^2} + U_{III,IV}(T_{III} - T_{IV}) \frac{1}{H_{IV}} + U_{IV,V}(T_V - T_{IV}) \frac{1}{H_{IV}} + \frac{j}{2F}\left(h_{H_2,V} + \frac{1}{2}h_{O_2,III} - h_{H_2O,IV}\right) \frac{1}{H_{IV}} + \alpha \frac{j}{F}\left(h_{H_2O,V} - h_{H_2O,IV}\right) \frac{1}{H_{IV}} - jV_{cell}\frac{1}{H_{IV}} \quad (22)$$

$$\lambda_{IV}\frac{\partial T_{IV}}{\partial x}\bigg|_{x=0} = U_{inf}(T_{IV} - T_{inf}) \quad \lambda_{IV}\frac{\partial T_{IV}}{\partial x}\bigg|_{x=L} = -U_{inf}(T_{IV} - T_{inf}) \quad (23)$$

Anode channel (V):

$$\frac{\partial C_V e_V}{\partial t} = -u_V \frac{\partial C_V h_V}{\partial x} - \frac{j}{2F} h_{H_2,V} \frac{1}{H_V} - \alpha \frac{j}{F} h_{H_2,V} \frac{1}{H_V} + U_{IV,V}(T_{IV} - T_V) \frac{1}{H_V} + U_{V,VI}(T_{VI} - T_V) \frac{1}{H_V} \quad (24)$$

$$T_V|_{x=0} = T^0_V \quad (25)$$

Anode side bipolar plate (VI):

$$\rho_{VI} c_{p,VI} \frac{\partial T_{VI}}{\partial t} = \lambda_{VI} \frac{\partial^2 T_{VI}}{\partial x^2} + U_{I,VI}(T_I - T_{VI}) \frac{1}{H_{VI}} + U_{V,VI}(T_V - T_{VI}) \frac{1}{H_{VI}} \quad (26)$$

$$\lambda_{VI}\frac{\partial T_{VI}}{\partial x}\bigg|_{x=0} = U_{inf}(T_{VI} - T_{inf}) \quad \lambda_{VI}\frac{\partial T_{VI}}{\partial x}\bigg|_{x=L} = -U_{inf}(T_{VI} - T_{inf}) \quad (27)$$

2.3. *Electrochemical model*

The electrochemical model addresses the calculation of the electrical performance of the PEM yielding the cells potential, current density profile and polarization losses. The adopted equation for calculating the cell voltage is taken from [23]:

$$V_{cell} = V_{OC} + \frac{RT_{IV}}{2F} \ln\left\{\frac{\left[P_{H_2}(x) - \left(\frac{\delta j(x)}{2FD_{H_2}}\right)\right] \times \left[P_{O_2}(x) - \left(\frac{\delta j(x)}{4FD_{O_2}}\right)\right]^{0.5}}{P_{H_2O}(x) + \left(\frac{\delta j(x)}{2FD_{H_2O}}\right)}\right\} - \frac{RT_{IV}}{F} \ln\left[\frac{j(x)}{j_0\left(P_{O_2}(x) - \frac{\delta j(x)}{4FD_{O_2}}\right)}\right] - \frac{j(x)t_m}{\sigma_m(x)} \quad (28)$$

It applies locally and takes into account ohmic losses (fourth term on the right-hand side), and diffusion and activation losses (lumped together into the second and third term on the right-hand side).

V_{oc} is the open circuit potential that occurs when zero current is delivered by the fuel cell and is calculated according to the Nernst equation:

$$V_{OC} = V^0 + \frac{RT_{IV}}{2F} \ln\left(\frac{P_{H_2} \cdot P^{0.5}_{O_2}}{P_{H_2O}}\right) \quad (29)$$

Regarding the ohmic losses, it is assumed that the membrane conductivity σ_m depends on the local membrane humidification based on the water content on the anodic side of the membrane $c_{w,a}$. The following empirical expression is adopted to determine σ_m in accord with [23–25]:

$$\sigma_m = \left(0.00514 \frac{W_{m,dry}}{\rho_{m,dry}} c_{w,a} - 0.00326\right) \exp\left[1268\left(\frac{1}{303} - \frac{1}{T_{IV}}\right)\right] \quad (30)$$

The model governing equation presented in sections 2.1 and 2.3, are implemented and solved using Aspen Custom Modeler package [20].

3. Fuel cell model validation

The model is validated on the basis of the characteristic curve presented in Ref. [23] assuming the same input parameters and operating data. Since no information is provided in terms of conditions of the cooling fluid, a mass flow of 5.5×10^{-5} kg s^{-1} and an inlet-outlet temperature variation of 5 °C are assumed, while the inlet temperature is set to maintain a fixed average temperature of the solid phase (sub-volume IV). The complete set of model input data is reported in Table 2.

The calculated PEM characteristic curves are reported in Fig. 2 and it shows good agreement with the reference data for a resulting average solid phase temperature $T_{IV,av}$ in a range between 85 and 95 °C.

Fig. 3 shows water transport through the membrane of the fuel cell as defined by Eq. (11), where the net flow of water molecules (α) is the result of the effect the osmotic drag (n_d) and back diffusion. The overall effect is a net migration of H_2O from the anode to the cathode side of the membrane. Values of α are significantly high near the entrance of the fuel cell due to the high partial pressure of water at anode stream (that enters the fuel cell is in saturated condition), in contrast to the dried cathode stream. The temperature distribution on the solid phase is provided on the right axis of Fig. 3. The water concentration along the anode side $c_{w,a}$ is depicted in Fig. 4 showing a marked influence on membrane conductivity and consequently on the current density distribution. It is worth noting that the water transport variables shown in Figs. 3 and 4 reflects those reported in Figs. 3 and 5 of Ref. [24] from where the cell physical parameters and operating conditions are obtained. Also the solid phase temperature distribution (Fig. 3) show a profile similar to that shown in Fig. 3(a) of reference [23].

4. Application to a mobile back up power supply

The fuel cell model described in the previous sections is employed to prove the feasibility of a PEM system for use as a back up power supply. For this purpose the actual electricity load of a computer file server (HP EX490 MediaSmart Server) was experimentally measured by a power measurement device (Watts Up Pro USB Power Analyzer [27]) over a period of 0.5 h. The power measurement device operates at 120 V AC at 60 Hz and records a maximum of 15 A. The unit has a measurement accuracy of +/− 1.5%. The registered load

Table 2 – Model input parameters [23,24].

Physical properties	
Membrane density, ρ_{dry}	2000 kg m^{-3}
Equivalent weight of dry membrane, $W_{m,dry}$	1100 kg kmol^{-1}
Water permeability, k_p	1.58 × 10^{-18} m^2
Intradiffusion coefficient of water in membrane D_0	5.5 × 10^{-11} m^{2}s^{-1}
H_2 diffusion coefficient, D_{H2}	10^{-10} m^{2}s^{-1}
H_{H2O} diffusion coefficient, D_{H20}	10^{-10} m^{2}s^{-1}
H_{O2} diffusion coefficient, D_{O2}	10^{-10} m^{2}s^{-1}
Exchange current density, A m^{-2}, j_0	100 A·m^{-2}
Bipolar plate heat capacity[a] $c_{p,I}$	1000 J kg^{-1}K^{-1}
Bipolar plate density[a] ρ_I	2000 kg m^{-3}
Bipolar plate thermal conductivity[a], λ_I	20 Jm^{-1}s^{-1}K^{-1}
Solid phase heat capacity $c_{p,IV}$	1000 J kg^{-1}K^{-1}
Solid phase density ρ_{IV}	2000 kg m^{-3}
Solid phase thermal conductivity, λ_{IV}	0.5 J m^{-1}s^{-1}K^{-1}
Convective heat transfer coefficient in flow channels, $U_{I,II}$, $U_{III,IV}$, $U_{IV,V}$, U_{inf}	250 J m^{-2}s^{-1}K^{-1}
Dimensions of the cell elements	
Cell length, L	100 mm
Cell width, W	1 mm
Fuel and air channel height, H_{III}, H_V	1 mm
Solid phase thickness, H_{IV}	0.1375 mm
Bipolar plate thickness[a] H_I	5 mm
Diffusion layer thickness, δ	0.01 mm
Membrane thickness, t_m	0.1275 mm
PEM operating parameters	
$M_{H2,V}$	1.14 × 10^{-5} mol·s^{-1}
$M_{H2O,V}$	Saturated condition
$T_{V,in}$	80 °C
$M_{O2,III}$	5.7 × 10^{-6} mol·s^{-1}
$M_{N2,III}$	0
$M_{H2O,III}$	0
$T_{III,in}$	80 °C
T_{inf}	70 °C
m^a_I	5.5 × 10^{-5} kg s^{-1}
ΔT_I[a]	5 °C

a Assumed in this paper.

profile is plotted in Fig. 5, resulting in an average power consumption of about 68 W. The PEM model is integrated with the necessary BoP components as shown in Fig. 6. Pure hydrogen is taken from the lithium hydride hydrogen storage

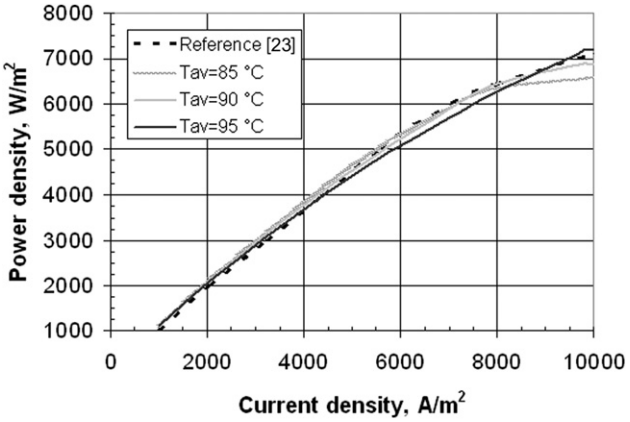

Fig. 2 – Comparison of the characteristic curve of the PEM with reference data for different resulting values of solid phase average temperature. Input data as by Table 2.

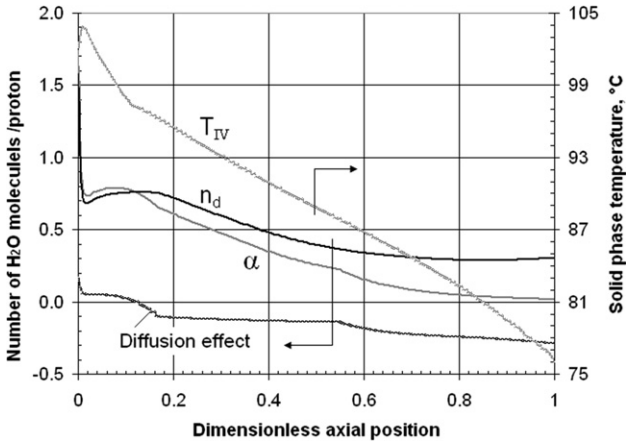

Fig. 3 – Distribution of PEM water transport variables (left axis) and temperature profile of the PEM solid phase (right axis). Input data as by Table 2.

(A) and is heated and humidified to conditions of 75 °C and 100% RH through the heater/humidifier component (B) before being fed to the PEM anode. A liquid water storage (C) provides the necessary H_2O for the release of hydrogen from the lithium hydride and for its humidification. The fuel valve (D) is employed to regulate the fuel mass flow according to the load power required, while the outlet fuel valve (E) provides the required backpressure to the anode channel and regulates the vented exhausts flow rate. Notably, when the valve is closed, the anode can operate in dead-end mode with the valve periodically opened to purge the anode of nitrogen buildup by blowing hydrogen through the line [28]. In order to reduce the auxiliary electricity consumption of the heater/humidifier – mainly due to the enthalpy of vaporization of the liquid water contained in the H_2O storage (C) – part of the required heat is recovered by cooling the cathode exhaust flow from 90 °C to 80 °C (in nominal condition). Ambient air is supplied from the air fan (F) moved by the inverter-fed electric motor (G) and is preheated to 50 °C through the recovery heat exchanger (H), before being fed to the PEM cathode. Two PIDs are added to the system: one (I) acts on the fuel valve opening, to maintain

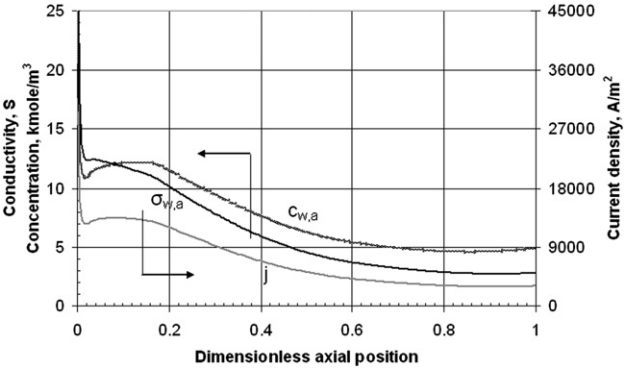

Fig. 4 – Profiles of water concentration at the anode side of the membrane ($c_{w,a}$), membrane conductivity (σ_m) and current density (j). PEM input data as by Table 2.

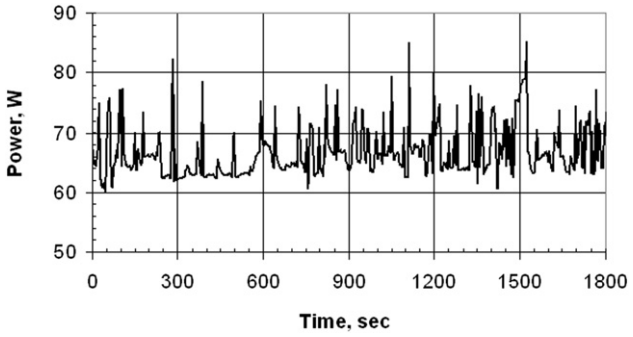

Fig. 5 – Measured power load of a computer file server (HP EX490 MediaSmart Server).

a constant fuel utilization factor of 85%; the other (J) regulates the power supplied to the air fan motor, thus varying the cathode air inlet mass flow to control the outlet temperature of the cathode stream. In fact, given the rather small size of the present fuel cell system, the heat can be removed by passing excess air over the air cathode avoiding any external cooling fluid. An auxiliary battery (K) is included into the system to supply electricity to the auxiliaries, leaving the fuel cell to provide only the power requested by the load. It also supplies the required power during fuel cell start up.

The fuel cell system shown in Fig. 6 is designed with reference to the nominal conditions, corresponding to the average power requested by the load of 68 W and for an operating time of 48 h. A preliminary design of the fuel cell and the main BoP components is given in the following. All the data are then summarized in Table 3.

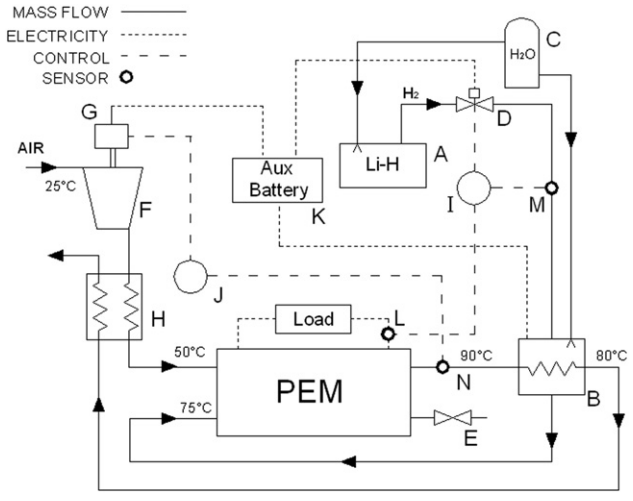

Fig. 6 – PEM system layout: (A) lithium hydride hydrogen storage, (B) fuel heater and humidifier, (C) liquid water storage, (D) fuel valve, (E) outlet fuel valve, (F) air fan, (G) air fan motor, (H) heat recovery air preheater, (I) fuel valve PID controller, (J) fan motor PID controller, (K) auxiliary battery, (L) current sensor, (M) H2 flow meter, (N) temperature sensor. Temperature data reported in the figure refer to nominal conditions.

Table 3 – Design data of the components of the PEM system. Data refers to the average load power of 68 W and to operating time of 48 h.

Fuel cell stack	
Current density	5000 $A \cdot m^{-2}$
Fuel utilization	85%
Fuel flow	2.36×10^{-05} $m^3 s^{-1}$ (H_2 with 100% RH)
Air flow	8.22×10^{-04} $m^3 s^{-1}$ (ambient air)
Anode input temperature	75 °C
Cathode input temperature	50 °C
Number of channels[a]	170
Resulting singe cell voltage	0.73 V
Hydrogen storage	
Technology	Lithium Hydride Hydrolysis [31]
Mass of lithium hydride	0.8 kg
Mass of water – no water recovered from FC	1.8 kg
Mass of water – 50% water recovered from FC	0.9 kg
Volume of fuel	1.3 lit (packed powder [31],)
Energy content	6.6 kWh
Heater/humidifier	
Mass of water consumed – no water recovered from FC	1.10 kg
Mass of water consumed – 50% water recovered from FC	0.55 kg
Gross energy consumption	772 Wh
Heat recovered from the cathode outlet	466 Wh
Net energy consumption	306 Wh
Air fan	
Air volume flow	8.2×10^{-4} $m^3 s^{-1}$
Rotational speed	8824 rpm
Power	0.511 W
Overall energy consumption	25 Wh
Auxiliary battery	
Technology	Lithium ion
Mass energy density	140 Wh kg^{-1}
Volume energy density	350 Wh lit^{-1}
Energy required to run the auxiliaries	330 Wh
Mass	2.4 kg
Volume	0.94 lit

a Channel dimensions are as by Table 2.

4.1. *Fuel cell*

The PEM nominal condition are set at 5000 A/m^2 with a fuel utilization of 85% (i.e. 15% of the H_2 supplied is eventually vented through the outlet valve). The single unit PEM channel considered in the model domain produces in these conditions a power of about 0.4 W. Thus a stack of 170 channels that can be arranged in 10 layers with 17 channels each, will provide the average power required by the load of 68 W. The PEM in these conditions operates with a hydrogen to electricity conversion efficiency of 49%, consistent with values that can be obtained in PEMs employed in similar applications [9–16]. The temperature profiles obtained in nominal conditions are reported in Fig. 7. It can be seen that the temperature of the cathodic air (T_c) progressively increases form 50 °C to 90 °C due

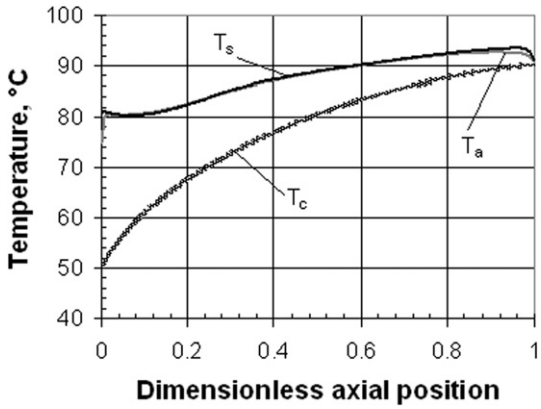

Fig. 7 – Temperature distribution along the anode channel (T_a) cathode channel (T_c) and solid structure (T_s) in case of PEM operated in nominal conditions of 5000 A/m^2 and fuel utilization of 85%.

to the heat removed from the fuel cell. As a result the temperature of the membrane (T_s) is maintained close to its optimum operating range. Fig. 8 shows the PEM electrical performance. The V_{OC} decrease as a consequence of the progressive reactant consumption according to Eq. (29). The contribution of ohmic, concentration and activation polarizations (Eq. (28)) are evidenced. The resulting operating cell voltage V_{cell} is about 0.73 V. Finally Table 4 reports a sensitivity analysis of the effect of the heat transfer coefficients ($U_{I,II}$, $U_{III,IV}$, $U_{IV,V}$, U_{inf}) on the PEM results. In this preliminary study they are fixed to 250 J m^{-2}s^{-1}K^{-1}, based on reference literature data [23–25]. It is shown that a variation from 100 to 400 J m^{-2}s^{-1}K^{-1}results in a decrease of the operating voltage form 0.79 to 0.67 V (second column of Table 4) and in a corresponding reduction of the PEM efficiency from 54% to 45% (third column). This in turn determines a progressive increase of the air mass flow (fourth column) necessary to remove the higher heat produced by the PEM. Given the significant influence on the PEM performances evidenced in this analysis, the flow channel dimensions, the gas velocities and their effect on the heat transfer coefficients need to be carefully evaluated in the design of the system.

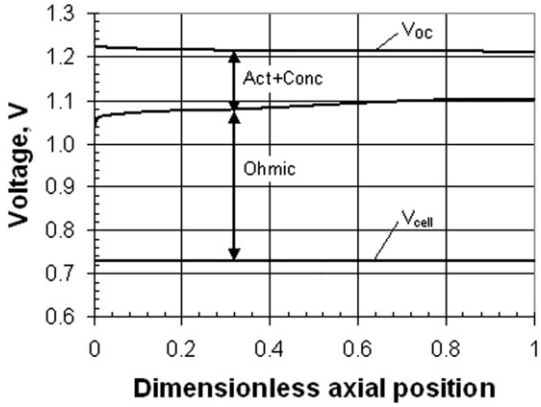

Fig. 8 – Open circuit potential V_{OC}, and polarization losses distribution in case of PEM operated in nominal conditions of 5000 A/m^2 and fuel utilization of 85%.

Table 4 – Influence of the assumed convective heat exchange transfer coefficients ($U_{I,II}$, $U_{III,IV}$, $U_{IV,V}$, U_{inf}) on the PEM model results. Reference case, as by Table 3, is in bold.

$U_{I,II}$, $U_{III,IV}$, $U_{IV,V}$, U_{inf}, J m^{-2}s^{-1}K^{-1}	PEM voltage, V	PEM efficiency, %	PEM air flow, m^3 s^{-1}
100	0.793	53.8	7.24×10^{-04}
150	0.774	52.5	7.53×10^{-04}
200	0.751	50.9	7.88×10^{-04}
250	**0.728**	**49.4**	**8.22×10^{-04}**
300	0.706	47.9	8.54×10^{-04}
350	0.686	46.5	8.85×10^{-04}
400	0.666	45.2	9.13×10^{-04}

4.2. *Air fan*

The air fan was selected among commonly available market products. Datasheet reference conditions are: volume flow $\dot{V}_{ref} = 6.5 \times 10^{-4}$ m^3/s, rotational speed $\omega_{ref} = 7000$ rpm and net power consumed $W_{ref} = 0.255$ W [29]. In nominal conditions the air volume flow required to fix the cathode exit stream to 90 °C is $\dot{V} = 8.2 \times 10^{-4}$ m^3/s. The corresponding rotational speed $\omega = 8824$ rpm and power consumed W = 0.511 W are obtained following the rules of similitude for turbomachinery

$$\omega = \omega_{ref}\frac{\dot{V}}{\dot{V}_{ref}} \tag{31}$$

$$W = W_{ref}\left(\frac{\omega}{\omega_{ref}}\right)^3 \tag{32}$$

As shown in the system layout (Fig. 6), the fan motor PID controller (J) varies the power supplied to the inverter-fed motor that drives the air fan, thus changing the rotational speed and the air mass flow to maintain the outlet temperature, measured by sensor N (Fig. 6), close to 90 °C.

From the power balance on the air fan shaft he have

$$J\frac{\partial\omega}{dt} = \frac{W_{motor}}{\omega} - \frac{W}{\omega} \tag{33}$$

where W_{motor} is the power supplied by the electric motor that drives the fan (PID controller output), W is the power necessary to drive the fan at a given speed according to Eq. (32) and J is the momentum of inertia.

Thus the dynamic equation of the air fan speed is obtained by substituting Eq. (32) into Eq. (33):

$$J\frac{\partial\omega}{dt} = \frac{W_{motor}}{\omega} - \frac{W_{ref}}{\omega_{ref}^3}\omega^2 \tag{34}$$

Given mass and dimensions of the air fan [29] the momentum of inertia was estimated to be 5×10^{-7} kg m^2.

4.3. *Fuel reservoir*

Different solution can be adopted for H_2 storage. These include high pressure bottles, various types of hydrogen chemical carriers (methanol, ammonia) reversible and non-reversible metal hydride [30]. The solution considered here is the hydrolysis of lithium hydride (a non reversible or chemical release metal hydride), as this option shows

significant mass savings compared to compressed hydrogen [31]. This option produces hydrogen on demand through hydrolysis of lithium hydride and water according to the chemical reaction [31]:

$$LiH + H_2O \rightarrow LiOH + H_2$$

The reaction is shown to be relatively simple to design, construct and control. In an earlier analysis carried out by the co-author [31] it was shown experimentally that by adopting an active feedback control system it is possible to control the lithium hydride release and maintain the lithium hydride chamber at a fixed pressure of 1.1 ± 0.01 bar. It is assumed that a similar apparatus is employed here so that from a modeling point of view the H_2 storage can be simulated as a tank kept at the fixed pressure of 1.1 bar.

4.4. *Fuel valve*

The fuel valve reduces the H_2 pressure to 1.02 bar at anode channel inlet. The model assumes that the pressure drop ΔP across the valve is related to hydrogen mole flow M_{H2} and the flow coefficient C_v according to the following general equation:

$$M_{H2} = C_v X \sqrt{\rho \Delta P} \tag{35}$$

where X is the degree of opening of the valve ($X = 0$ when the valve is closed, $X = 1$ when full opened). The fuel valve PID controller operates on the valve opening position X to maintain the fuel utilization to 85%. The fuel utilization is defined as

$$U_f = \frac{\frac{i}{2F}}{M_{H2}} \cdot 100 \tag{36}$$

where the fuel mole flow M_{H2} and the cell current i are measured by sensors M and L respectively (Fig. 6). Any inertia of the valve mechanism is neglected so that the valve opening reaches instantly the opening value X set by the PID.

4.5. *Heater-humidifier*

To maintain the membrane well hydrated the fuel inlet flow is fed into the anode channel in condition of 100% RH at 75 °C. Liquid water for humidification is assumed to be supplied from an external source and is then injected into the H_2 flow and evaporated through the heater/humidifier. The heat required for the H_2O evaporation is provided through electricity supplied by the auxiliary battery. Thus to reduce the size of the auxiliary battery, part of the requested heat is recovered by cooling the cathode exit stream from 90 °C to 80 °C (in nominal conditions). It is worth to note that part of the water necessary for the fuel humidification as well as for the hydrolysis of lithium hydride can also be recovered from the cell outlet streams. This option, with a slight complication of the BoP, carries the advantage of a reduced size of the H_2O storage which however results to be a secondary aspect in the present application.

Table 5 – PIDs tuning parameters.

Variable	Fan motor PID controller	Fuel valve PID controller
Proportional gain	3.2	20
Integral time	5	1
Derivative time	0	0.5

4.6. *Auxiliary battery*

An overall energy of 330 Wh is necessary to run the auxiliary components of the system for 48 h. The resulting battery based on Li-ion technology has mass and volume of 2.4 kg and 0.94 lit respectively. It is worth noting that about 93% of the BoP energy consumption is due to the heater/humidifier.

5. Results and discussion

Numerical simulations of the system layout shown in Fig. 6 are carried out by applying to the fuel cell the load profile shown in Fig. 5. The aim of this analysis is to determine an effective control strategy that allows the fuel cell to operate under load changes in optimized conditions with fuel utilization of 85% and with the cathode outlet temperature close to the nominal value of 90 °C. To this purpose the controllers parameters reported in Table 5 have been determined by manual tuning. The manual tuning method used to obtain values for the controller uses Ziegler–Nichols tuning method as a starting point. However there are key differences in the controller processes that require additional modifications. Initially all tuning parameters for the fan controller are set to zero and the ultimate gain is determined to calculate K_p (proportional gain) and K_i (integral time), using a PI controller as per the Ziegler–Nichols method. However for this study, there is frequent source of external disturbance due to the stochastic, high and varying power demands, that in turn results in unacceptably high temperature oscillations in the system. This requires increasing the K_i value much higher than Ziegler–Nichols would suggests to eliminate or further reduce the steady-state errors caused by external disturbances quickly. Under ideal conditions where there is no external disturbance, increasing K_i further would eliminate steady state errors, however in this situation, this will only minimize error due to accumulated

Table 6 – Sensitivity analysis on the effect of the number of fuel cell intervals on the accuracy of the results. Cell voltages refers to the steady-state nominal conditions as by Table 3.

Number of intervals	Cell voltage, V	Expected error, %
4	0.863	18.9
5	0.833	14.7
6	0.814	12.1
10	0.799	10.1
15	0.773	6.5
20	0.760	4.7
50	0.738	1.7
100	0.731	0.7
200	0.728	0.3
400	0.726	–

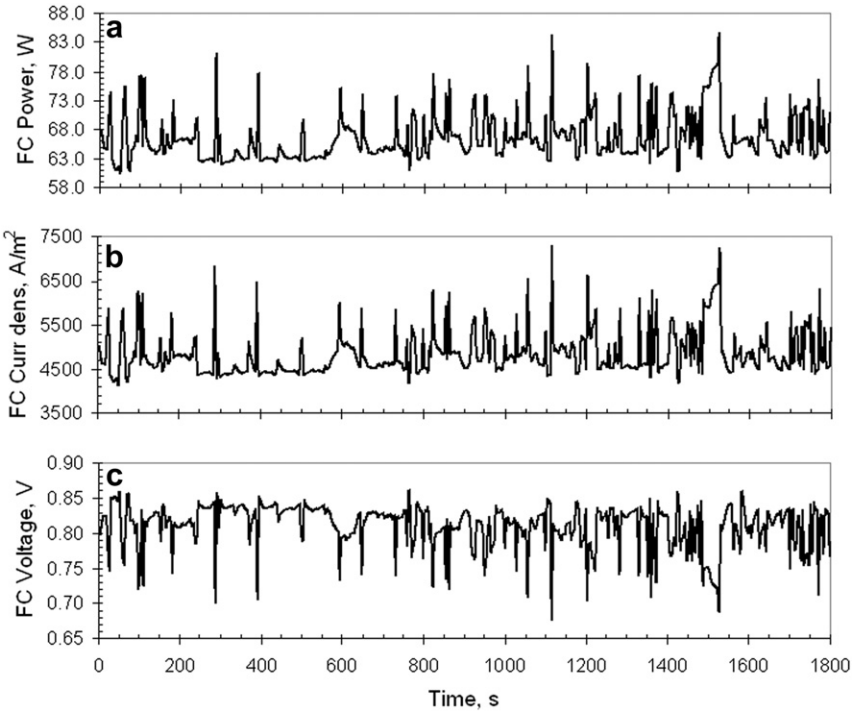

Fig. 9 – Fuel cell power (a), current density (b) and voltage (c) time profiles.

external disturbances. Tuning of both these parameters was sufficient to meet the fan controller control goal of +/− 3 °C most of the time. A similar process was followed for obtaining a fuel valve controller. First the gain was set to the ultimate gain and all other parameters were zeroed to determine K_p and K_i according to Ziegler–Nichols for a PI controller. Using the Ziegler–Nichols values for a PI control it was observed caused some instability during our testing. Therefore, the K_d (derivative time) value was tuned until the observed instability was eliminated. While both manual tuning approaches show acceptable controller performance for the given study, these parameters are subject to change if there is a substantial difference in the disturbance profile (i.e. oscillations in input load). However once a different disturbance profile is identified, then the process is straightforward to once again tune the controller parameters. In fact the ease with which these controllers can be tuned suggests, this could be implemented as an online algorithm that would perform automatic adjustment of the controller parameters, particularly K_i (integral time) and K_d (derivative time) when the fan temperatures oscillates above the +/− 3 °C.

Table 6 reports the accuracy of the simulations as a function of the number of intervals in which the fuel cell domain is divided in the axial direction (i.e. along the cell).[1] Although a high number of intervals is beneficial to the accuracy of the calculation, a trade off is necessary to achieve an acceptable computational time. In the present analysis it was chosen to use 10 intervals in order to keep below 50 h the computational time required for the 0.5 h real time simulation.[2] An Euler implicit integrator method with variable time step was adopted. According to Table 6 the expected error on the fuel cell voltage and power is about 10%.

Results of the simulations are reported in Figs. 9–11 suggesting the following comments:

- the current profile (Fig. 9b) follows the varying load power (Fig. 9a) with maximum and minimum value of 7300 and 4100 A/m^2 respectively. As expected, the voltage undershoots and overshoots (Fig. 9c) are opposite to those of the current. Notably the voltage drops below 0.7 V only for a few seconds, maintaining its value in a desirable operating range, as far as the degradation of the cell is concerned.
- the valve opening regulated by the PID fuel valve (Fig. 10b) allows the fuel utilization to vary within ±1% of the set point value of 85% (Fig. 10a).
- similarly, Fig. 11a shows that the cathodic outlet temperature is effectively controlled by varying the power supplied to the air fan (controller output of the fan motor PID, Fig. 11b) thus regulating the rotational speed (Fig. 11c) and the cathodic air flow according to Eqs. (31)–(33). This results in a variation within ±3 °C of the set point value of 90 °C for most of the time. The only exception occurs at sec 1530 where the load abruptly decreases from 84 to 65 W in 4 s resulting in a drop of temperature to a minimum value of 83 °C. As a consequence the controller acts with a rapid reduction of the power supplied to the air fan (Fig. 11b) causing a reduction of its speed (Fig. 11c). This in turn determines a peak of

[1] Previous steady state calculations (results in Figs. 2–4, 7 and 8) are carried out considering the unit cell divided into 250 intervals. A further increase of the number of intervals has negligible effects on the accuracy of the results.

[2] All runs were performed on a PC with 2.4 GHz and 2 GB RAM.

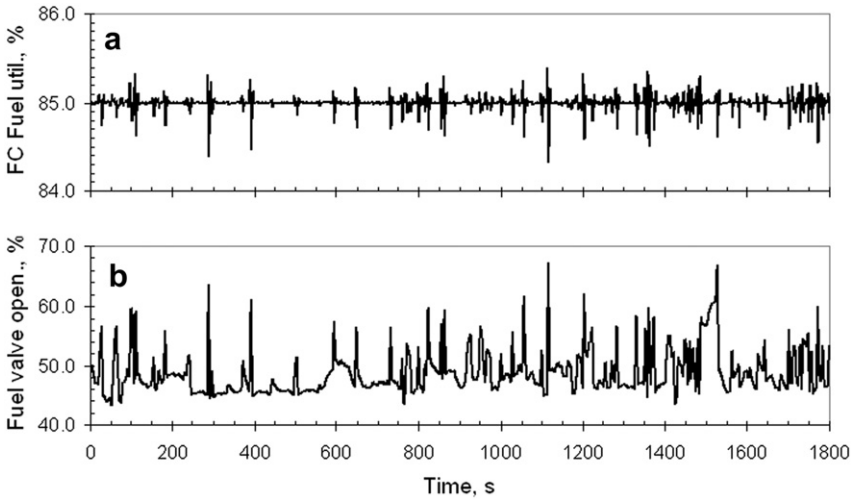

Fig. 10 – Effect of the fuel valve opening (b) (controller output of the fuel valve PID) on the PEM fuel utilization (a).

97 °C, in correspondence to the subsequent increase of power load. Nonetheless, after the two temperature peaks, the set point temperature of 90 °C is reached in about 18 s and the overall period where the temperature exceeds the limit of ±3 °C of the nominal value is less than 50 s.

5.1. *Expected fuel cell life and comparison with battery back up power supply*

The backup power supply considered in this study, under the stated operating conditions could, according to co-author's model on PEM fuel cell catalyst degradation [32], operate for approximately 13,000 h of continuous operation. However it is expected that a backup power supply would be used very infrequently, with a worst case of 48 h of continuous usage at a time. Assuming the fuel cells have to be started and stopped every time, then the net fuel cell start/stop cycle life is expected to be about 200 [33], with 48 h of operating time during each cycle, giving an operational life of 9600 h over 200 start/stop cycles.

In contrast, battery backup power supplies are limited because they need to be constantly charged by external power sources, until its used. Current silver zinc and lithium ion

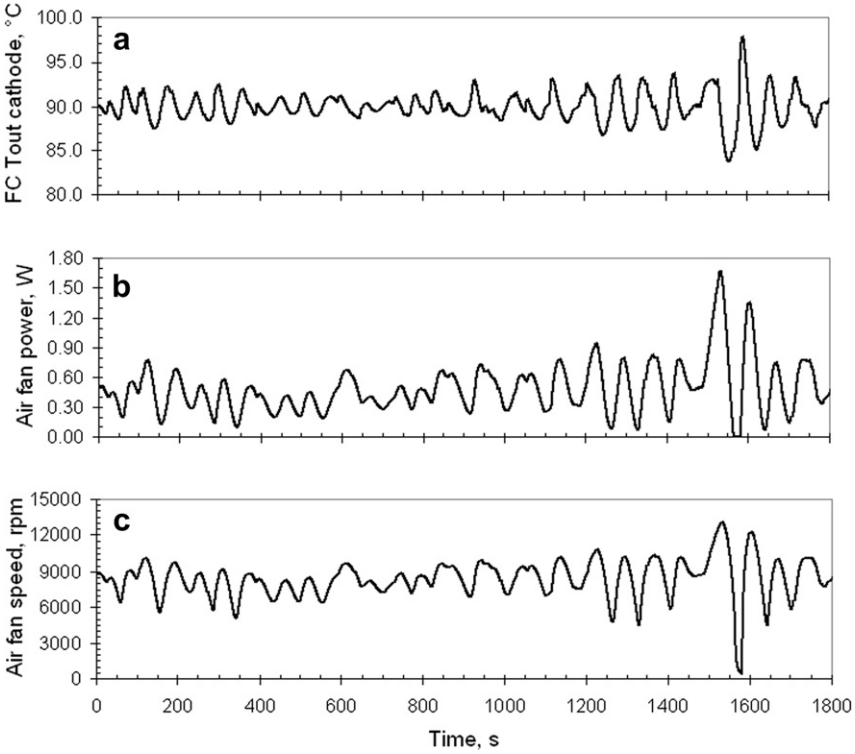

Fig. 11 – Effect of the air fan power (b) (controller output of the air fan PID) on the air fan speed (c) and on the PEM cathode outlet temperature (a).

batteries typically have to be replaced after 2–3 years, regardless of whether it ever intervened and provided backup power. In contrast, a fuel cell backup power supply in theory has a life of 200 such interventions. Scenarios in which there is short but frequent power cuts, a battery backup power supply might be the best option. However when there is long but infrequent power cuts, the fuel cell backup power supply offers a better solution than conventional batteries.

6. Conclusions

This paper reports the study of a mobile power backup for uninterruptable power units based on a PEM fuel cell. A preliminary design of the main components is carried out in view of an operating time of 48 h. In this system the fuel cell is fed by pure hydrogen taken from a lithium hydride hydrogen storage while ambient air is supplied to the cathode by an air fan moved by the inverter-fed electric motor. A dynamic model of the system including the PEM fuel cell and the relevant component of the balance of plant is developed and implemented in Aspen Custom Modeler. The fuel cell is modeled through a finite difference approach where mass and energy balance equations are applied locally together with the pertinent equations of the electrochemical model yielding the profiles of any relevant thermodynamic and electrochemical cell variable.

The actual electricity load of a computer file server (HP EX490 MediaSmart Server) was experimentally measured by a power measurement device over a period of 0.5 h and applied to the fuel cell model. Dynamic and control simulations are carried out including use of two PIDs controllers in the system: one acting on the fuel valve opening to maintain a constant fuel utilization factor of 85% and the other regulating the power supplied to the air fan motor, thus varying the cathode air inlet mass flow to control the outlet temperature of the cathode stream to the set point value of 90 °C.

Results of the simulations shows that with an appropriate choice of the PID's setting parameters, obtained through hand tuning, we obtained a robust control system that maintains the variables within the desired set point targets with acceptable oscillations. In particular the valve opening regulated by the PID fuel valve allows the fuel utilization to vary within ±1% of the set point value of 85% while the cathodic outlet temperature is effectively controlled by varying the power supplied to the air fan, resulting in a variation within ±3 °C of the set point value of 90 °C for most of the time.

Acknowledgement

Paolo Iora gratefully acknowledges the Cariplo-UniBS-MIT-MechE faculty exchange program co-sponsored by UniBS and the CARIPLO Foundation, Italy under grant 2008-2290.

Notation

a_k	water activity in channel k
$C_{i,j}$	molar concentration of component i in sub-volume j, mol m^{-3}
c_p	specific heat capacity, J $kg^{-1}\cdot K^{-1}$
C_v	valve flow coefficient
$c_{w,k}$	water concentration at k interface of the membrane, mol m^{-3}
D	diffusion coefficient in diffusion layer, $m^2\ s^{-1}$
D_0	intradiffusion coefficient of water in membrane, $m^2\ s^{-1}$
D^*	diffusion coefficient of water in membrane, $m^2\ s^{-1}$
e_i	specific internal energy of channel i, J mol^{-1}
F	Faraday's constant, C mol^{-1}
H_i	height of sub-volume i, m
h_i	specific enthalpy of channel i, J mol^{-1}
$h_{i,j}$	specific enthalpy of specie i at condition of channel j, J mol^{-1}
I	current, A
j_0	exchange current density, A m^{-2}
j	local current density A m^{-2}
J	momentum of inertia, kg m^2
k_p	water permeability, m^2
L	length of the fuel cell, m
m_{cool}, m_l	coolant mass flow, kg s^{-1}
n_d	electro-osmotic coefficient of water in membrane (molecules/protons)
M_i	molar flow rate of species i, mol s^{-1}
$M^v{}_{w,k}$	molar flow rate of water vapor in k channel, mol s^{-1}
MEA	Membrane Electrode Assemblies
OCV	Open Circuit Potential
P	pressure, bar
$P_{w,k}$	water partial pressure in channel k, bar
Q_{conv}	convective thermal power, kJ s^{-1}
R	gas constant, J mol^{-1} K^{-1}
RH	relative humidity
t	time, s
t_m	membrane thickness, m
T	temperature, K
u	velocity, m s^{-1}
U	heat transfer coefficient, $Jm^2\ s^{-1}$ K^{-1}
U_f	fuel utilization
UPS	Uninterruptable Power Supply
V^0	open circuit potential in standard conditions, V
V_{cell}	cell operating potential, V
V_{OC}	open circuit potential, V
$\dot{V}$	volume flow, $m^3\ s^{-1}$
x	axial coordinate
$x_{w,k}$	molar fraction of water in vapour phase in k channel
X	degree of fuel valve opening
W	power, W; width, m
$W_{m,dry}$	membrane dry weight, kg $kmol^{-1}$

Greek letters

α	ratio of water molecules per H^+ proton flux, molecules/proton
δ	diffusion layer thickness, m
λ	thermal conductivity, J $m^{-1}\ s^{-1}\ K^{-1}$
μ	water viscosity, kg $m^{-1}\ s^{-1}$
ω	rotational speed, rad s^{-1}
ρ	density, kg m^{-3}
$\rho_{m,dry}$	dry membrane density, kg m^{-3}
σ_m	membrane conductivity, $\Omega^{-1}m^{-1}$

Subscripts

a	anode
av	average
c	cathode
el	electric
inf	surroundings
ref	reference
s	solid phase

Superscripts

0	cell inlet condition
sat	saturation

REFERENCES

[1] Larminie J, Dicks A. Fuel cell systems explained. Chichester, England: Wiley; 2003.
[2] O'Hayre R, Cha SW, Colella W, Prinz FB. Fuel cell fundamentals. New York: John Wiley & Sons; 2006.
[3] Endo E. Market penetration analysis of fuel cell vehicles in Japan by using energy system model MARKAL. International Journal of Hydrogen Energy 2007;32:1347–54.
[4] Campanari S, Macchi E, Manzolini G. Membrane reformer PEMFC cogeneration systems for residential applications – Part A: full load and partial load simulation. Asia-Pacific Journal of Chemical Engineering 2009;4(3):301–10.
[5] Campanari S, Macchi E, Manzolini G. Membrane reformer PEMFC cogeneration systems for residential applications – Part B: techno-economic analysis and system layout. Asia-Pacific Journal of Chemical Engineering 2009;4(3):311–21.
[6] Dyer CK. Fuel cells for portable applications. Journal of Power Sources 2002;106:31–4.
[7] Tuber K, Zobel M, Schmidt H, Hebling C. A polymer electrolyte membrane fuel cell system for powering portable computers. Journal of Power Sources 2003;122:1–8.
[8] Squadrito G, Giacoppo G, Barbera O, Urbani F, Passalacqua E, Borello L, et al. Design and development of a 7kW polymer electrolyte membrane fuel cell stack for UPS application. International Journal of Hydrogen Energy 2010; 35:9983–9.
[9] Chang HP, Chou CL, Chen YS, Hou TI, Wheng BJ. The design and cost analysis of a portable PEMFC UPS system. International Journal of Hydrogen Energy 2007;32:316–22.
[10] Lin M, Cheng Y, Lin M, Yen S. Evaluation of PEMFC power systems for UPS base station applications. Journal of Power Sources 2005;140:346–9.
[11] Gonzales J, Tamizhmani G. High efficiency fuel cell based uninterruptible power supply for digital equipment. Journal of Power Sources 2006;153:151–6.
[12] Segura F, Durán E, Andújar JM. Design, building and testing of a stand alone fuel cell hybrid system. Journal of Power Sources 2009;193:276–84.
[13] Zhan Y, Wanga H, Zhu J. Modelling and control of hybrid UPS system with backup PEM fuel cell/battery. Electrical Power and Energy Systems 2012;43:1322–31.
[14] Jiang ZH, Gao LJ, Blackwelder MJ, Dougal RA. Design and experimental tests of control strategies for active hybrid fuel cell/battery power sources. Journal of Power Sources 2004;130:163–71.
[15] Choi W, Howzeb JW, Enjeti P. Fuel-cell powered uninterruptible power supply systems: design considerations. Journal of Power Sources 2006;157:311–7.
[16] Varkaraki E, Lymberopoulos N, Zoulias E, Guichardot D, Poli G. Hydrogenbased uninterruptible power supply. International Journal of Hydrogen Energy 2007;32:1589–96.
[17] Bernardinis AD, Péra MC, Garnier J, Hissel D, Coquery G, Kauffmann JM. Fuel cells multi-stack power architectures and experimental validation of 1 kW parallel twin stack PEFC generator based on high frequency magnetic coupling dedicated to on board power unit. Energy Conversion and Management 2008;49(8):2367–83.
[18] Panos C, Kouramas KI, Georgiadis MC, Brandon N, Pistikopoulos EN. Modelling and explicit MPC of PEM fuel cell systems. 20th European Symposium on Computer Aided Process Engineering; 2010.
[19] Tao WQ, Min CH, Liu XL, He YL, Yin BH, Jiang W. Parameter sensitivity examination and discussion of PEM fuel cell simulation model validation. Part I. Current status of modeling research and model development. Journal of Power Sources 2006;160:359–73.
[20] Aspen Custom Modeler V7.1. 200 Wheeler Road Burlington, MA 01803 USA: Aspen Technology, Inc; 2009.
[21] Iora P, Aguiar P, Adjiman CS, Brandon NP. Comparison of two IT DIR-SOFC models: impact of variable thermodynamic, physical, and flow properties. Steady-state and dynamic analysis. Chemical Engineering Science 2005;60:2963–75.
[22] Iora P, Campanari S. Development of a three dimensional molten carbonate fuel cell model and application to hybrid cycle simulations. Journal of Fuel Cell Science and Technology 2007;4:501–10.
[23] Golbert J, Lewin DR. Model-based control of fuel cells: (1) Regulatory control. Journal of Power Sources 2004;135:135–51.
[24] Yi JS, Nguyen TV. An along-the-channel model for proton exchange membrane fuel cells. Journal of Electrochemical Society 1998;145:1149–59.
[25] Meidanshahi V, Karimi G. Dynamic modeling, optimization and control of power density in a PEM fuel cell. Applied Energy 2012;93:98–105.
[26] Nguyen TV, White RE. A water and heat management model for proton-exchange-membrane fuel cells. Journal of Electrochemical Society 1993;140:2178–86.
[27] Watt's Up Pro USB power measurement device specification sheet https://www.wattsupmeters.com/secure/products.php?pn=0&wai=0&spec=3 [accessed 10.08.12].
[28] Siegel JB, Bohac SV, Stefanopolou AG, Yesilyurt S. Nitrogen front evolution in purged polymer electrolyte membrane fuel cell with dead-ended anode. Journal of Electrochemical Society 2010;157:1081–93.
[29] http://www.adda.com.tw/data/file/AD2010.pdf [accessed 08.04.12].
[30] Vielstich W, Gasteiger HA, Lamm A, editors. Handbook of fuel cells-fundamentals, technology and applications. Fuel cell technology and applications, vol 3. John Wiley & Sons, Ltd, ISBN 0-471-49926-9; 2003.
[31] Thangavelautham J, Strawser D, Cheung M, Dubowsky S. Lithium hydride powered PEM fuel cells for long-duration small mobile Robotic Missions. 2012 IEEE International Conference on Robotics and Automation (ICRA), St. Paul, Minnesota; 2012.
[32] Thangavelautham J, Dubowsky S. Controlling degradation in fuel cell power supplies for long life mobile field sensor networks. Journal of Fuel Cells: Fundamental to Systems 2012:1–28.
[33] Yu PT, Gu W, Makharia R, Wagner FT, Gasteiger HA. The impact of carbon stability on PEM fuel cell startup and shutdown voltage degradation. Electrochemical Society Transactions 2006;3(1):797–809.